Journal of Catalysis 396 (2021) 192–201

Contents lists available at ScienceDirect

Journal of Catalysis

journal homepage: www.elsevier.com/locate/jcat

Importance of the oxyl character on the IrO_2 surface dependent catalytic activity for the oxygen evolution reaction

Danilo González [1], Javier Heras-Domingo [1], Mariona Sodupe, Luis Rodríguez-Santiago, Xavier Solans-Monfort *

Departament de Química, Universitat Autònoma de Barcelona, 08193 Bellaterra, Spain

ARTICLE INFO

Article history:
Received 13 November 2020
Revised 20 February 2021
Accepted 22 February 2021
Available online 04 March 2021

Keywords:
Oxygen evolution reaction
IrO_2
Metal-oxyl species
DFT

ABSTRACT

The oxygen evolution reaction catalyst optimization is hindered because in the desirable acidic conditions the sole active catalysts are RuO_2 and IrO_2. Thus, the understanding of the factors controlling the reactivity of these materials is mandatory. In this contribution, DFT (PBE-D2) periodic calculations are performed to analyze the catalytic activities of the main ((110), (011), (100) and (001)) IrO_2 surfaces. Results show that the reaction only occurs if the Ir=O species on the surfaces exhibit an oxyl character. The water nucleophilic attack mechanism is the most favorable pathway on the (110), (100) and (001) surfaces. In contrast, for the (011) facet the oxo-coupling is preferred. The required overpotentials for the four IrO_2 surfaces depend on the feasibility to oxidize the Ir-OH to Ir-O species and this is tuned by the coordination of the unsaturated iridium sites: the (100) and (001) surfaces appear to be more active than the (110) and (011).

1. Introduction

One of the major challenges of the 21st century is the substitution of fossil fuels for sustainable and environmentally friendly alternative sources of energy [1,2]. One of the most promising solutions is to store energy in the form of chemical bonds in a similar manner to what plants do during the photosynthesis [3]. In this way, H_2 production by the splitting of water is seen as one of the most sustainable ways to store energy [4–11].

Water splitting implies two half reaction: i) At the cathode, H^+ are converted to H_2 through the hydrogen evolution reaction (HER) and ii) H_2O is oxidized to O_2 through the oxygen evolution reaction (OER), at the anode. The OER is considered the bottleneck of the global process due to the large overpotentials that have to be applied. Moreover, acidic conditions are preferred with respect to basic media for the practical application of water splitting [12,13]. However, these acidic media also imply working at harsh reaction conditions which limits the number of potential catalysts to the expensive IrO_2 and RuO_2 [13–15]. In this context, understanding the key factors controlling catalyst efficiency is essential to find strategies that could lead to catalyst optimization.

Regarding the catalytic performances of different IrO_2 materials, it has been found that the crystalline (100) surface is more active than the crystalline (110) one.[16] These different catalytic activities correlate reasonably well with the number of undercoordinated centers per surface area of the crystalline facets [17]. Therefore, this suggests that the undercoordinated centers are the main active sites in crystalline materials. Moreover, amorphous IrO_X tends to be more active, [18–22] but less stable than the crystalline analogues, the deactivation mechanisms being a key issue under discussion.[20,23,24]

In-situ X-ray spectroscopy has been carried out to identify the oxidation state of the metal center as function of the applied potential.[18,20,25–30] For IrO_2, many authors showed that while at potentials below 1.3 V, the metal centers are mainly Ir(IV) or Ir(III), at higher potentials they are oxidized to Ir(V).[25,31] The Ir(V) species are proposed to be involved in the catalytic process and they are probably reduced upon O_2 release.[26] The data for the most stable (110) surface is consistent with the IrO_2 being completely covered with *O (oxo) species coordinated to the unsaturated centers at reaction conditions (C in Scheme 1).[28] In addition, Infrared spectroscopy (FT-IR) allowed the detection of Ir-OOH species (D in Scheme 1) upon water oxidation with an IrO_2 nanocluster under pulsed excitation of a light sensitizer.[32] Finally, the use of differential electrochemical mass spectroscopy (DEMS) with isotope-labeled electrolytes showed that IrO_2 exchanges oxygen with the electrolyte and thus actively partici-

* Corresponding author at: Departament de Química, Universitat Autònoma de Barcelona, Carrer dels Til·lers s/n, 08193 Bellaterra, Spain.
E-mail address: xavier.solans@uab.cat (X. Solans-Monfort).
[1] D.G. and J. H.-D. have equally contributed.

https://doi.org/10.1016/j.jcat.2021.02.026
0021-9517/

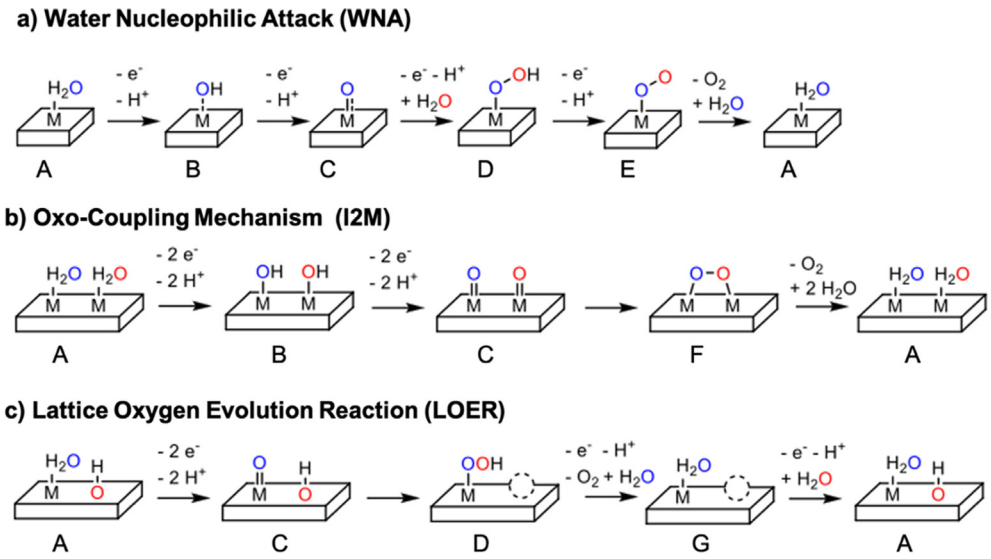

Scheme 1. Proposed reaction mechanisms for the Oxygen Evolution Reaction.

pates in the catalysis through its lattice oxygen atoms.[20,33,34] Nevertheless, according to the most recent results of Shao-Horn and co-workers on RuO_2, this would be the case of none-crystalline materials, since no oxygen exchange is detected on rutile-like catalysts.[13,17]

Three different reaction mechanisms have been proposed (Scheme 1):[12,13,35,36] i) the water nucleophilic attack (WNA), ii) the oxo-coupling mechanism (I2M) and iii) The lattice oxygen evolution reaction mechanism (LOER). The water nucleophilic attack mechanism (Scheme 1a) implies first the formation of an Ir-oxo species on the surface (Ir=O) through two proton coupled electron transfer steps (PCET). Then, the Ir=O species suffers the attack of a water molecule leading to the formation of an Ir-OOH hydroperoxo species that after one additional PCET releases O_2 and regenerates the initial Ir-H_2O species. The I2M pathway (Scheme 1b) starts also with the formation of Ir=O species, but, in contrast to the WNA mechanism, O_2 is formed by the coupling of two neighbor Ir=O species. Finally, the LOER mechanism (Scheme 1c) implies the active role of vacant sites on the metal oxide surface[20,33,34], but their role in highly crystalline materials, as the surfaces considered in this work, appears to be less significant.[13,17]

Computational chemistry has been widely used to shed light into the most plausible reaction mechanism.[37–57] This is mainly done by computing the thermodynamic cost of each PCET step. Only in a few cases, the energy barriers associated with some of the elementary steps have been computed[38,40,55,58] Remarkably, most of the studies focusing on the reaction mechanism are centered on the most stable (110) surface.[37–40,49,51–55,574 1–44] Only a very recent contribution of Rao et al. analyzed the differences in catalytic activity of the (110), (100) and (101) surfaces of RuO_2.[45] Despite the limitations in solvent representation among others,[39,40] the computed overpotentials are in good agreement with experiments and they support that the WNA mechanism is usually the applied mechanism. Indeed, in the crystalline (110) surface the water nucleophilic attack to the oxo-species is computed to be kinetically easier than the oxo-coupling of the I2M.[38,40,55] Noteworthily, in some flexible systems such as oxidized iridium surfaces or supported dimeric Ir species, the I2M mechanism has been suggested to be competitive with the WNA one.[46,47,53] Taking WNA as the applying mechanism, three different rate determining steps have been proposed: i) The Ir=O formation (B to C step in Scheme 1); ii) the electrochemical step associated with the Ir-OOH formation (C to E step in Scheme 1) and iii) O_2 release from Ir-OOH (E to A in Scheme 1). Controversy persists, and one can find recent contributions suggesting that either the formation of Ir-OOH or the O_2 release are the rate determining processes.[53,55,57]

In this contribution we report a computational study on the catalytic activity of IrO_2 main crystallographic surfaces (110), (011), (100) and (001), with the aim of determining if all low miller index facets share the same most favorable reaction mechanism and rate determining step and understanding the reactivity differences. For that, we include the energy barriers of the water nucleophilic attack and oxo-coupling chemical steps. Moreover, the analysis of the electronic structure of the major intermediates allows proposing an alternative chemical description of the chemical steps.

2. Computational details

The main IrO_2 surfaces were represented with the slab models used in our previous contributions (Fig. 1).[59,60] They were built by considering a (2x2) supercell, cut from the optimized bulk structure. All slabs present a four-layer thickness to ensure a reasonable converged surface energy.[59,60] The c value was set to 35 Å, the interlayer distance being at least 21 Å. During the optimizations, cell parameters were kept fix, while the atom positions were fully relaxed.

All DFT periodic boundary calculations were performed with the spin polarized formalism as implemented in the VASP code [61,62] and using the GGA PBE functional.[63] Grimme's D2 empirical correction was added to account for dispersion forces.[64] D2 correction leads to bulk cell parameters that are closer to the experimental data than those obtained with D3.[59,60] Ionic cores were described with projector augmented wave pseudopotentials [65,66] and the valence electrons were represented through a plane wave basis with a kinetic energy cut off of 500 eV. A (4,4,1) Monkhorst – Pack K-point mesh[67] was employed to describe the first Brillouin zone. The energy convergence criteria were fixed to 10^{-5} and 10^{-4} eV for electronic and geometry relaxations, respectively. This methodology is equivalent to that used in our previous contributions on RuO_2 and IrO_2 materials.[59,60,68]

Solvation effects were included by using the implicit model implemented in VASPsol[69] through single point calculations at vacuum optimized geometries. Thermal corrections at 1 atm and

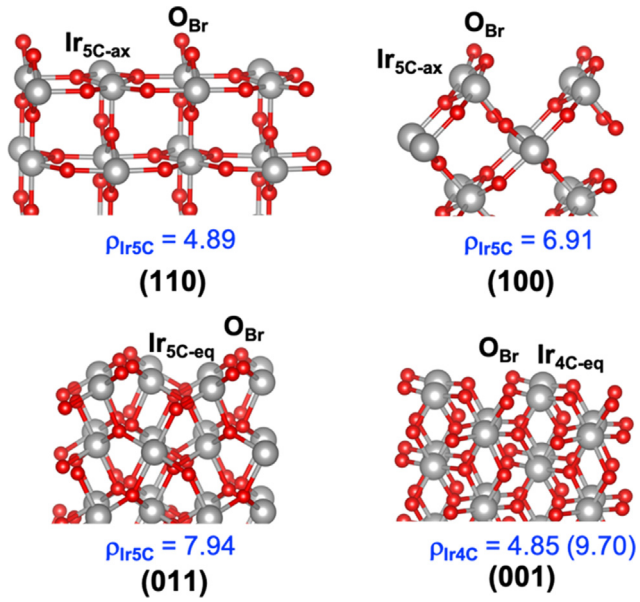

Fig. 1. Surfaces considered in this work. $\mathbf{O_{br}}$ refers to the unsaturated surface oxygen atoms. $\mathbf{Ir_{5C\text{-}ax}}$ and $\mathbf{Ir_{5C\text{-}eq}}$ stands for pentacoordinated iridium centers presenting an axial and equatorial vacant site respectively. $\mathbf{Ir_{4C\text{-}eq}}$ are tetracoordinated iridium sites with two equatorial vacant sites. The density of undercoordinated Ir centers per nm^{-2} (blue values) is also included.

T = 273 K were added considering only the vibrational contributions of the normal modes associated with the adsorbed species and the Ir-O_{ads} stretching mode. Entropy contributions for water and H_2 were obtained from the tabulated values for liquid water and H_2 gas, respectively. Similarly to previous contributions, [37,53–55] the O_2 Gibbs energy was computed as the energy difference between the experimental $\Delta G°$ of the global reaction (4.92 eV for $2H_2O \rightarrow 2\ H_2 + O_2$) and the Gibbs energies of H_2O and H_2 as shown in equation 1. No particular treatment was applied to $\mathbf{5_{OH/OO}}$ and $\mathbf{6_{O/OO}}$ as the analysis of the electronic structure suggest a superoxide (O_2^{-}) character with only one single unpaired electron. Finally, the $\Delta G°$ for the PCET steps were computed by using the computational standard hydrogen electrode as defined by Rossmeisl, Nørskov and co-workers.[37]

$$G^{o}_{O2} = 4.92 + 2\ G^{o}_{H2O} - 2\ G^{o}_{H2}\ (\text{in eV}) \quad (1)$$

Transition states for the oxo-coupling and water nucleophilic attack chemical steps were located by using either the climbing image nudged elastic band (CI-NEB)[70,71] strategy or restricted geometry optimizations. The highest in energy point of either the NEB or the restricted optimization was used for locating the final transition state by performing a geometry optimization with the quasi-Newton algorithm implemented in VASP. Convergence was achieved when forces were smaller than 0.02 eV/Å. The nature of the stationary point was ensured by vibrational analysis that showed that the largest imaginary frequency in all cases corresponds to that of the transition state.

We also performed calculations on (2x1) supercells models of the (110), (100) and (001) surfaces as well as a (1x1) model of the (011) facet to ensure that the density of Ir=O groups has no effect on the main conclusions. In these four models all iridium centers on the surface are fully oxidized. As shown in Table S1 of the Supplementary Material, there are some differences associated with the adsorption of water and its oxidation to OH that arise from cooperative hydrogen bonding between water molecules in the models with higher water coverages. However, the computed overpotentials for the four surfaces and the two explored mechanism are similar (differences smaller than 0.2 V and 0.1 V for the I2M and the WNA mechanisms, respectively) and the reaction energies of the O-O bond formation either through the oxo-coupling or the water nucleophilic attack mechanisms show little variations (less than 0.2 eV). Therefore, results are not model dependent.

3. Results and discussion

We have studied the oxygen evolution reaction catalyzed by the main ((110), (011), (100) and (001)) crystallographic facets of rutile-like IrO_2, with the aim of analyzing their different catalytic activity. In this context, we first determine the potentials required for oxidizing the initial IrO_2-H_2O material to Ir=O without involving additional water molecules and analyze the electronic structure of the Ir-OH and Ir=O intermediates. In a second step, we compute the catalytic cycle of the two most usually proposed mechanisms (oxo-coupling and water nucleophilic attack) starting from the most stable termination at 1.5 V. We do not consider the LOER mechanism since, according to experiments, it appears to be less relevant in defective free materials such as the models used here. This allows us determining the most favorable mechanism, proposing the rate determining electrochemical step and computing the overpotentials.

3.1. IrO_2–H_2O oxidation as a function of the applied potential

Fig. 2 shows the most stable conformation associated with H_2O adsorption on the different surfaces. Rutile-like IrO_2 structure presents a distorted octahedral environment around the metal center with two short Ir-O distances in axial position and four long ones in the equatorial plane. The most stable (110) surface and the (100) facet present unsaturated pentacoordinated metal sites with the vacant site in axial position. The second most stable (011) surface has also unsaturated pentacoordinated metal sites but with the vacant site in equatorial. Finally, the least stable main crystallographic orientation, (001), presents tetracoordinated unsaturated metal centers, the two vacant sites being equatorial. In addition, all surfaces present non-saturated dicoordinated oxygen atoms (O_{br}). We recently showed that the different nature of the vacant at metal center, the basicity of the oxygen bridge atoms and the hydrogen bonding between adsorbed water molecules influence the adsorption strength of a single water molecule and its facility to dissociate forming an Ir-OH moiety and a protonated oxygen bridge.[59,60,72–74] For IrO_2, the adsorption energies are the highest when the vacant site is axial and the most stable structures are: complete dissociation on the (110) and (100) surfaces and 50% or lower dissociation on the other two surfaces (Fig. 2). At this point it is worth mentioning that, although at least one water molecule dissociates in the majority of cases, the initial species will hereafter be referred as $\mathbf{0_{H2O/H2O}}$ for simplicity.

The oxidation of $\mathbf{0_{H2O/H2O}}$ to $\mathbf{4_{O/O}}$ is expected to occur through successive PCET steps. The final species has vicinal Ir=O as shown in Scheme 2. With the aim of stablishing the most stable termination as a function of the applied potential (U) at pH = 0, we represented the relative stabilities of all species in Fig. 3, obtained by using equation 2, where $\mathbf{N_{L1/L2}}$ stands for the considered species $\mathbf{1_{OH/H2O}}$, $\mathbf{2_{OH/OH}}$, $\mathbf{3_{O/OH}}$ and $\mathbf{4_{O/O}}$.

$$\mathbf{0}_{H2O/H2O} \rightarrow \mathbf{N}_{L1/L2} + ne^{-} + nH^{+}\ \Delta G^{0} = G^{0}_{N} - G^{0}_{0} - nU \quad (2)$$

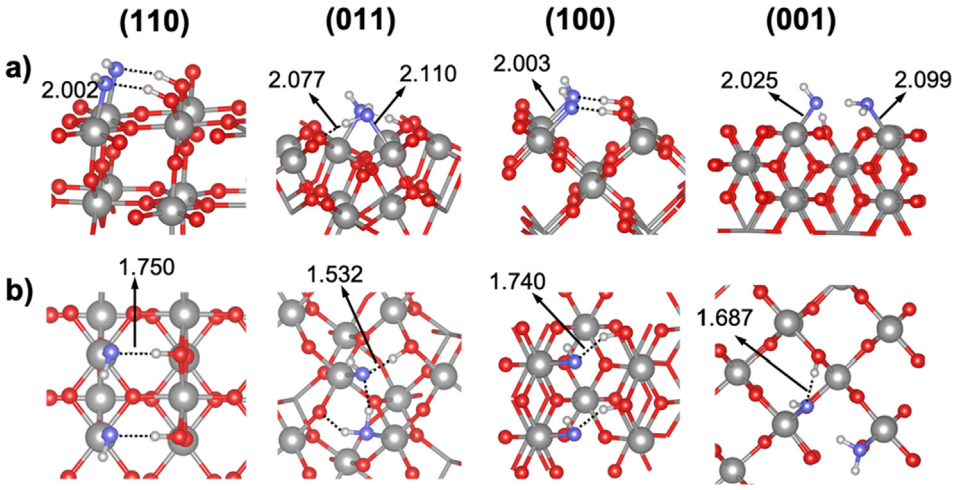

Fig. 2. Lateral (a) and apical (b) view of the most stable structures for the adsorption of two water molecules on the main IrO_2 surfaces. Distances in Å.

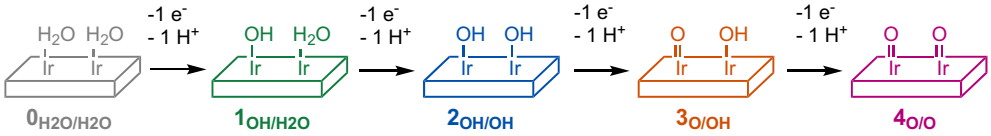

Scheme 2.

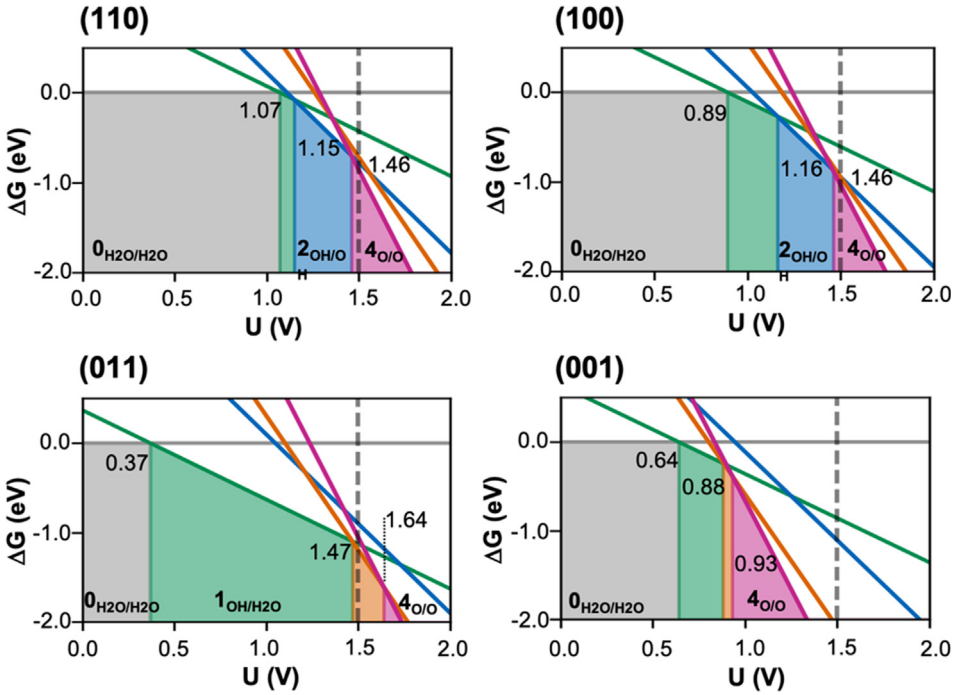

Fig. 3. Surface phase diagram of IrO_2 at pH = 0, T = 298 K and P = 1 atm as a function of the applied potential. Grey stands for $\mathbf{0_{H2O/H2O}}$, green stands for $\mathbf{1_{OH/H2O}}$, blue stands for $\mathbf{2_{OH/OH}}$, orange stands for $\mathbf{3_{O/OH}}$ and pink for $\mathbf{4_{O/O}}$.

Three different oxidation behaviors are observed. The (001) surface is more easily oxidized to $\mathbf{4_{O/O}}$ than the other facets, the potentials at which $\mathbf{4_{O/O}}$ becomes the most stable termination being 0.93 V. The other three surfaces present pentacoordinated centers and they behave in a more similar manner. However, the ability of the different surfaces to get oxidized depends also on the vacant site nature. The (110) and (100) surfaces have the vacant site in axial position, and they get oxidized to $\mathbf{2_{OH/OH}}$ at potentials of 1.15–1.16 V and to $\mathbf{4_{O/O}}$ at potentials over 1.46 V. The (011) surface, with the vacant site in the equatorial plane, is not easily oxidized to $\mathbf{4_{O/O}}$, which is only predicted to be the most favorable species over 1.64 V. As a consequence, at potentials around 1.5 V, $\mathbf{4_{O/O}}$ is still not formed and $\mathbf{3_{O/OH}}$ is the most stable termination. These values agree well with the computational data

for the (110) surface reported by Ping, Nielsen and Goddard.[55] Moreover, the $\mathbf{2_{OH/OH}}$ to $\mathbf{4_{O/O}}$ transition is computed to occur at 1.46 V, which is only 0.16 V higher than the potential in which iridium is oxidized to its higher state according to experiments.[25] Thus, there is a fairly good agreement between our data and the existent values, which reinforces the validity of our approach.

Geometric parameters (Table 1 and Supplementary Material) show that the Ir-O_L distance (O_L stands for the oxygen of the adsorbed species) decreases when going from Ir-H_2O to Ir-OH and Ir=O. Moreover, the Ir-O_L distance tends to be shorter for the (001) surface than for the (110) and (100) facets, the (011) surface usually showing the largest values. This is clearly observed for $\mathbf{4_{O/O}}$ where the shortest distances are those of the (001) surface and the largest ones those of the (011) facet. Interestingly, the shortest distance in the (001) surface is related with the absence of magnetic moment over the oxo ligand (Table 1), thus suggesting the formation of an oxo group with an Ir=O double bond and a metal center formally at its +6 oxidation state. In contrast, the larger distances of the (110), (100) and (011) are associated with unpaired electrons both on the metal and the oxo. This indicates that such species have an important metal oxyl $Ir^{\bullet}$–$O^{\bullet}$ radical character where the metal oxidation state is formally +5 (Table 1). This interpretation is in agreement with the proposal that Ir(V) species are the ones involved in the catalytic cycle[26] and the observation of oxyl species on iridium surfaces by means of X-Ray spectroscopy and it suggest that the reactivity of the (001) surface could be different to that of the other three facets.

In summary, the oxidation of these facets is largely controlled by the coordination of the unsaturated metal centers and the nature of their vacant sites. The least coordinated tetracoordinated centers of the (001) surface are the least stabilized ones and, consequently, those that more easily form the Ir=O group. Within the other three surfaces, the nature of the vacant site appears to be the key factor: Ligands at axial sites present stronger interactions than ligands at equatorial sites. Moreover, the oxo group (or oxyl radical) interacts more strongly than water with the metal center. Consequently, the decrease in strength when going from axial vacant sites ((110) and (100) facets) to an equatorial one ((011)) is more pronounced for Ir=O, the latter becoming destabilized with respect to $\mathbf{0_{H2O/H2O}}$ and thus, requiring higher potentials to be formed.

3.2. OER reaction mechanism

Starting from the most stable termination at potentials of 1.5 V ($\mathbf{4_{O/O}}$ for the (110), (100) and (001) surfaces and $\mathbf{3_{OH/O}}$ for the (011) surface), we have studied the two most commonly proposed reaction mechanisms (Scheme 3): the oxo-coupling (I2M) and the water nucleophilic attack (WNA). The lattice oxygen evolution reaction mechanism (LOER) was not considered, since, according to experiments, it does not take place in a significant manner in defective free materials.[17] For each pathway, we computed the thermodynamics of the whole cycle as well as the energy barriers associated with the chemical steps. Table 2 reports the energetics of the different steps at 0 V potential versus standard hydrogen electrode (SHE).[37] Table 3 presents the main geometry parameters and spin densities of the key intermediates and Figs. 4 and 5 show the optimized structures of the transition states. All other data can be found in the Supplementary Material.

The first step of the I2M mechanism is a chemical process in which two oxo species on the surface couple forming an O-O bond (oxo coupling $\mathbf{4_{O/O}}$ to $\mathbf{4_{O\text{-}O}}$). The global process is endergonic for all IrO_2 main crystallographic facets, the reaction energies ranging between 0.10 and 2.30 eV. The most unfavorable oxo-coupling occurs at the (001), where the Ir=O species has the most pronounced oxo character. The least unfavorable process takes place at the (011), where the two Ir=O species are closer (2.887 Å) and the Ir=O species is less stabilized with respect to two adsorbed water molecules. The energy barriers for this step show that the reaction is kinetically more challenging for the (001) surface, followed by the (100) and (110) facets and the (011) surface being the one with the lowest barrier. Indeed, the process is only accessible at the (011) surface ($\Delta G^{\ddagger}$ = 0.33 eV), where oxidation of $\mathbf{3_{OH/O}}$ to $\mathbf{4_{O/O}}$ is needed prior to the oxo-coupling. This process requires potentials above 1.64 V to take place.

Analysis of reactants, products and transition states' structures shows that during the oxo–coupling process the O···O distance decreases to 1.387–1.404 Å in $\mathbf{4_{O\text{-}O}}$ and this is associated with an elongation of the Ir-O bond (2.012–2.043 Å). The computed O-O distance in $\mathbf{4_{O\text{-}O}}$ suggests that O_2 acts as μ-η^1:η^1-O_2^{2-} peroxo ligand coordinated to two metal centers[75,76] and this is in agreement with the absence of spin moment over the oxygen atoms. Thus,

Table 1
Ir-O_L distances (in Å) and spin moment for the different surface terminations arising from the oxidation of hydrated IrO_2 (110), (011), (100) and (001) surfaces.

Species	Ir_1-O_{L1}	Ir_2-O_{L2}	S_{O1}	S_{O2}	S_{Ir1}	S_{Ir2}
	(110)					
$\mathbf{0_{H2O/H2O}}$	2.002	2.002	0.00	0.00	0.00	0.00
$\mathbf{1_{OH/H2O}}$	1.943	1.990	0.00	0.00	0.00	0.00
$\mathbf{2_{OH/OH}}$	1.937	1.938	0.00	0.00	0.00	0.00
$\mathbf{3_{OH/O}}$	1.788	1.925	0.54	0.02	0.48	0.15
$\mathbf{4_{O/O}}$	1.789	1.789	0.67	0.67	0.52	0.52
	(011)					
$\mathbf{0_{H2O/H2O}}$	2.110	2.077	0.00	0.00	0.00	0.00
$\mathbf{1_{OH/H2O}}$	1.953	2.148	0.00	0.00	0.00	0.00
$\mathbf{2_{OH/OH}}$	1.965	1.940	0.00	0.00	0.00	0.00
$\mathbf{3_{OH/O}}$	1.810	1.933	0.57	0.02	0.55	0.00
$\mathbf{4_{O/O}}$	1.797	1.797	0.59	0.62	0.52	0.57
	(100)					
$\mathbf{0_{H2O/H2O}}$	2.003	2.003	0.02	0.02	0.08	0.12
$\mathbf{1_{OH/H2O}}$	1.951	1.958	0.01	0.01	0.20	0.15
$\mathbf{2_{OH/OH}}$	1.927	1.927	0.17	0.17	0.41	0.40
$\mathbf{3_{OH/O}}$	1.796	1.924	0.19	0.02	0.24	0.03
$\mathbf{4_{O/O}}$	1.771	1.771	0.57	0.56	0.26	0.26
	(001)					
$\mathbf{0_{H2O/H2O}}$	2.025	2.099	0.00	0.00	0.02	0.01
$\mathbf{1_{OH/H2O}}$	1.947	2.094	0.00	0.00	0.00	0.00
$\mathbf{2_{OH/OH}}$	1.933	1.900	0.00	0.00	0.00	0.00
$\mathbf{3_{OH/O}}$	1.729	1.898	0.00	0.00	0.00	0.00
$\mathbf{4_{O/O}}$	1.732	1.727	0.00	0.00	0.00	0.00

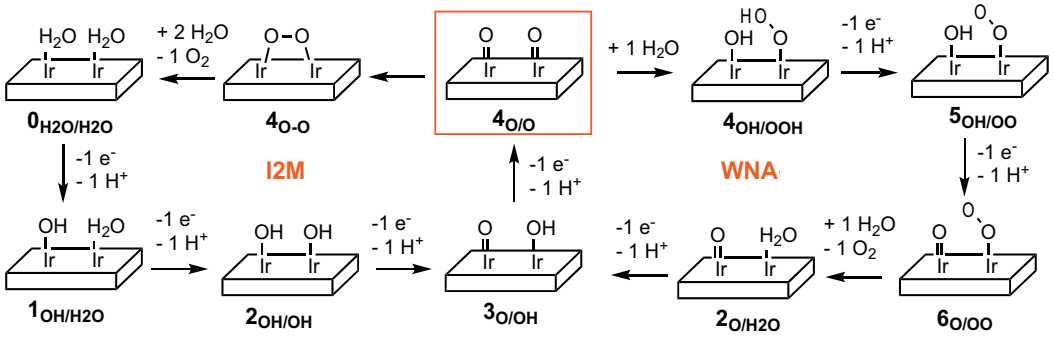

Scheme 3.

Table 2
Reaction Gibbs Energies (in eV) for the chemical and electrochemical steps of the I2M and WNA reaction mechanisms. Values in parenthesis correspond to the Gibbs energy barriers. Reaction conditions are 0 V potential versus SHE, pH = 0, T = 298 K and P = 1 atm.

Reaction	(110)	(011)	(100)	(001)	(001)_1c[a]
	I2M				
$\mathbf{4_{O/O}} \rightarrow \mathbf{4_{O-O}}$	0.67 (0.80)	0.10 (0.33)	0.85 (0.94)	2.30 (2.38)	0.25 (1.15)
$\mathbf{4_{O-O}} + 2H_2O \rightarrow \mathbf{0_{H2O/H2O}} + O_2$	−0.89	−0.13	−0.90	−0.72	−0.11
$\mathbf{0_{H2O/H2O}} \rightarrow \mathbf{1_{OH/H2O}} + H^+ + e^-$	1.07	0.37	0.90	0.64	0.83
$\mathbf{1_{OH/H2O}} \rightarrow \mathbf{2_{OH/OH}} + H^+ + e^-$	1.15	1.73	1.16	1.25	1.10
$\mathbf{2_{OH/OH}} \rightarrow \mathbf{3_{O/OH}} + H^+ + e^-$	1.56	1.21	1.50	0.52	1.38
$\mathbf{3_{O/OH}} \rightarrow \mathbf{4_{O/O}} + H^+ + e^-$	1.36	1.64	1.41	0.93	1.47
	WNA				
$\mathbf{4_{O/O}} + H_2O \rightarrow \mathbf{4_{OH/OOH}}$	−0.12 (0.43)[b]	−0.05 (0.42)[b]	0.08 (0.42)[b]	1.24	0.25 (0.55)[b]
$\mathbf{4_{OH/OOH}} \rightarrow \mathbf{5_{OH/OO}} + H^+ + e^-$	1.11	0.85	1.22	0.84	1.20
$\mathbf{5_{OH/OO}} \rightarrow \mathbf{6_{O/OO}} + H^+ + e^-$	1.53	1.52	1.22	0.91	1.24
$\mathbf{6_{O/OO}} + H_2O \rightarrow \mathbf{2_{O/H2O}} + O_2$	−0.17	−0.02	−0.40	0.56	−0.21
$\mathbf{2_{O/H2O}} \rightarrow \mathbf{3_{O/OH}} + H^+ + e^-$	1.21	0.98	1.37	0.76	0.97
$\mathbf{3_{O/OH}} \rightarrow \mathbf{4_{O/O}} + H^+ + e^-$	1.36	1.64	1.41	0.93	1.47

[a] **(001)_1c** stands for the OER on one single iridium center of the (001) surface.
[b] The reaction energy is computed as $G_{solv}(4_{OH/OOH}) - (G_{solv}(4_{O/O}) + G_{solv}(H_2O))$, while the Gibbs energy barrier is computed from an intermediate species ($\mathbf{4_{O/O\text{-}H2O}}$) where one water molecule is interacting with $\mathbf{4_{O/O}}$. The Gibbs energy difference between $\mathbf{4_{O/O}} + H_2O$ and $\mathbf{4_{O/O\text{-}H2O}}$ is always lower than 0.10 eV.

Table 3
Ir-O_L distances (in Å) and spin moments for the reaction intermediates of the I2M and WNA mechanisms.

Species	Ir_1-O_{L1}	Ir_2-O_{L2}	O-O	S_{L1}	S_{L2}	S_{Ir1}	S_{Ir2}
	(110)						
$\mathbf{4_{O/O}}$	1.789	1.789	3.182	0.67	0.67	0.53	0.53
$\mathbf{4_{O-O}}$	2.024	2.022	1.395	0.00	0.00	0.00	0.00
$\mathbf{4_{OOH/OH}}$	1.931	1.913	1.417	0.00	0.10	0.00	−0.10
$\mathbf{5_{OO/OH}}$	1.931	1,896	1.297	0.22	0.10	−0.10	−0.10
$\mathbf{6_{OO/O}}$	1.923	1.781	1.289	−0.15	−0.31	0.12	−0.17
	(011)						
$\mathbf{4_{O/O}}$	1.797	1.797	2.887	0.62	0.59	0.57	0.52
$\mathbf{4_{O-O}}$	2.043	2.016	1.404	0.00	0.00	0.00	0.00
$\mathbf{4_{OOH/OH}}$	1.961	1.936	1.446	0.00	0.00	0.00	0.00
$\mathbf{5_{OO/OH}}$	1.983	1.939	1.293	0.63	0.00	−0.12	0.00
$\mathbf{6_{OO/O}}$	1.941	1.798	1.281	0.08	0.57	−0.04	0.54
	(100)						
$\mathbf{4_{O/O}}$	1.771	1.771	3.187	0.50	0.50	0.34	0.34
$\mathbf{4_{O-O}}$	2.012	2.015	1.395	−0.02	−0.02	0.01	0.01
$\mathbf{4_{OOH/OH}}$	1.927	1.914	1.406	0.00	0.00	0.00	0.00
$\mathbf{5_{OO/OH}}$	1.958	1.912	1.286	−0.63	0.03	0.17	−0.02
$\mathbf{6_{OO/O}}$	1.932	1.760	1.287	−0.43	−0.05	0.12	−0.01
	(001)						
$\mathbf{4_{O/O}}$	1.732	1.732	4.304	0.00	0.00	0.00	0.00
$\mathbf{4_{O-O}}$	2.033	2.033	1.387	0.00	0.00	0.00	0.00
$\mathbf{4_{OOH/OH}}$	1.885	1.895	1.464	0.00	0.00	0.00	0.00
$\mathbf{5_{OO/OH}}$	1.853	1.889	1.280	0.00	0.00	0.00	0.00
$\mathbf{6_{OO/O}}$	1.856	1.726	1.273	0.00	0.00	0.00	0.00

the $\mathbf{4_{O/O}}$ to $\mathbf{4_{O-O}}$ process should be viewed as the homolytic coupling of two oxyl groups, without reduction of the metal center at the surface.

Once the peroxide is formed, the subsequent steps are accessible at reaction conditions. The ligand exchange between O_2 and two water molecules is in all cases exergonic with reaction ener-

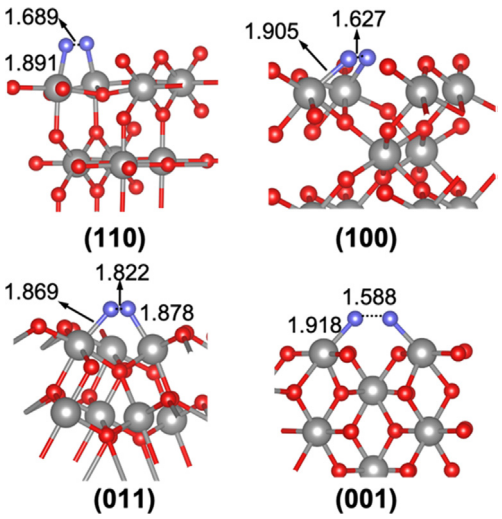

Fig. 4. Transition states of the oxo-coupling chemical step. Distances in Å.

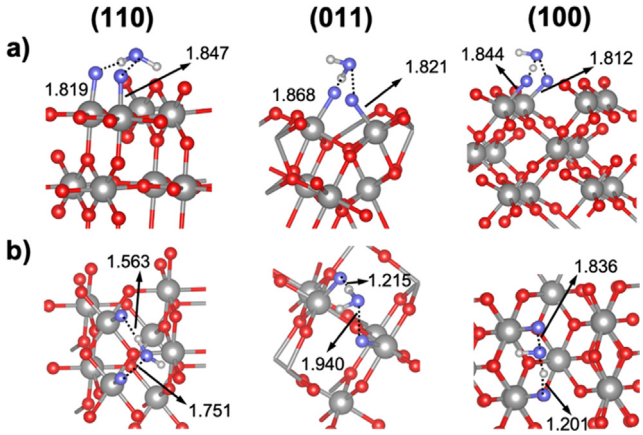

Fig. 5. Lateral (a) and apical (b) view of the transition states associated with the water nucleophilic attack chemical step on the main IrO_2 surfaces. Distances in Å.

gies between −0.13 and −0.90 eV. This formally reduces the metal center and regenerates $\mathbf{0_{H2O/H2O}}$ that as discussed in the first section can be easily reoxidized to $\mathbf{4_{O/O}}$ at potentials of 1.5 V with the exception of the (011) surface. Consequently, the electrochemical steps of the I2M mechanism in the (110), (100) and (001) are accessible at working potentials. However, in these three surfaces, this reaction mechanism is hampered by the energy cost of the chemical oxo–coupling step. The I2M mechanism at the (011) surface appears to be chemically feasible (energy barrier of 0.33 eV), but this surface is not easily oxidized and thus higher overpotentials would be required.

From $\mathbf{4_{O/O}}$, the WNA mechanism starts with a step where water reacts with the surface. This process has been proposed to occur either in a concerted manner or in two steps. In the first case, the H^+ is transferred to the solution and the OH couples with Ir=O implying the transfer of one electron to the electrode.[40] In the second case, H_2O initially dissociates on the surface through a chemical process that is followed by a proton coupled electron transfer [58,77] For the (110) surface, these pathways have been reported to present low energy barriers. Here, we considered that water initially dissociates as H^+/OH^- at two oxo sites at the surface, forming $\mathbf{4_{OOH/OH}}$. Despite the other possibilities may be competitive or even preferred, the here obtained values can be used as indicative of the feasibility of the water nucleophilic attack. The reaction energies associated with the $\mathbf{4_{O/O}}$ to $\mathbf{4_{OOH/OH}}$ chemical step are within −0.12 and 1.24 eV (-11.6 and 119.6 kJ mol^{-1}). The reaction is slightly exergonic at the (110) (-0.12 eV), essentially isergonic at the (011) and (100) surfaces (-0.05 and 0.08 eV, respectively) and highly unfavorable at the (001) surface (1.24 eV). The Gibbs energy barriers from an intermediate structure where the water molecule interacts through hydrogen bonding with the two Ir=O species are in all cases low (around 0.42 – 0.43 eV) except for the (001) surface where the process is thermodynamically hampered, and we were not able to localize the transition state.

The Ir-O distances at $\mathbf{4_{OOH/OH}}$ are similar to those computed for $\mathbf{2_{OH/OH}}$ and indicative of an Ir-O single bond. Moreover, the O-O distance in the Ir-OOH species ranges from 1.406 to 1.464 Å. These geometry features are associated with the absence of magnetization in any of the three oxygens of Ir-OOH and Ir-OH species, thus suggesting that Ir-OOH should be viewed as a hydroperoxo (OOH^-) species[75]. According to this sequential pathway the H_2O dissociation should be viewed as an homolytic splitting of water, which allows understanding the role of the oxyl character on the surface. That is, when $\mathbf{4_{O/O}}$ shows an important oxyl character such as on the (110), (011) and (100) surfaces the process is accessible and follows a reasonable correlation (Figure S2 of the Supplementary Materials). In contrast, the Ir=O species in the (001) surface is mainly an oxo group and the H_2O attack is forbidden.

From $\mathbf{4_{OOH/OH}}$, two PCET steps ($\mathbf{4_{OOH/OH}}$ to $\mathbf{5_{OO/OH}}$ and $\mathbf{5_{OO/OH}}$ to $\mathbf{6_{OO/O}}$) take place before the release of O_2 occurs. While the O_2 release is a favorable chemical process, the two proton transfers are challenging. The $H^+ + e^-$ transfer from $\mathbf{4_{OOH/OH}}$ involves the H from the hydroperoxo and it is electrochemically accessible on all surfaces at relatively low potentials.[78] The two resulting Ir-O distances in $\mathbf{5_{OO/OH}}$ are similar to those of $\mathbf{2_{OH/OH}}$ and $\mathbf{4_{OOH/OH}}$, thus suggesting a single bond (See Tables 1 and 3). Moreover, the O-O distance of the originally OOH^- species shortens (from about 1.4 to about 1.3 Å) and the magnetization on the OO increases. This is indicative of the formation of $O_2^{-\bullet}$ and thus, the oxidation takes place at the O_2-based ligand. The $\mathbf{5_{OO/OH}}$ to $\mathbf{6_{OO/O}}$ step is in all cases more unfavorable than the $\mathbf{4_{OOH/OH}}$ to $\mathbf{5_{OO/OH}}$ one. The geometrical parameters as well as the spin distribution on the ligands of $\mathbf{6_{OO/O}}$ suggest that Ir-O has an important oxyl character on the (110) and (011) facets, with a relatively large Ir-O distance. In contrast, Ir=O is best viewed as an oxo group on the (100) and (001) surfaces. Since the iridium oxo bond (Ir=O) is stronger than the iridium oxyl one ($Ir^{\bullet}$-$O^{\bullet}$), the $\mathbf{5_{OO/OH}}$ to $\mathbf{6_{OO/O}}$ step becomes particularly challenging for the (110) and (011) surfaces, where the required potentials are higher than 1.5V.

In summary, the WNA mechanism is accessible for the (110), (011) and (100) surfaces at reaction conditions. Despite the required overpotentials for the WNA and I2M mechanisms are similar within each particular surface, the Gibbs energy barrier for O-O bond formation indicates that the WNA is the preferred mechanism on the surfaces presenting iridium atoms with an axial vacant site ((110) and (100)). In contrast, the I2M pathway is preferred on the (011) surface where the vacant site of underoordinated iridium centers is equatorial. Finally, the (001) surface does not seem to be reactive if two metal centers are required to achieve the process and this is associated with the formation of Ir=O oxo species.

We decided to explore if OER could occur on one single Ir center of the (001) surface, taking into account that Ir is tetracoordinated and has two vacant sites on this surface. Results are summarized on Fig. 6 and Table 2. Formation of two Ir-O groups requires overcoming higher potentials than those involved for the formation of one single oxo group. However, the computed values are lower than 1.5 eV. This suggests that bisoxo species on the (001) are expected to be formed at reaction conditions. Moreover, structural analysis indicates that the two oxo groups present Ir-O distances

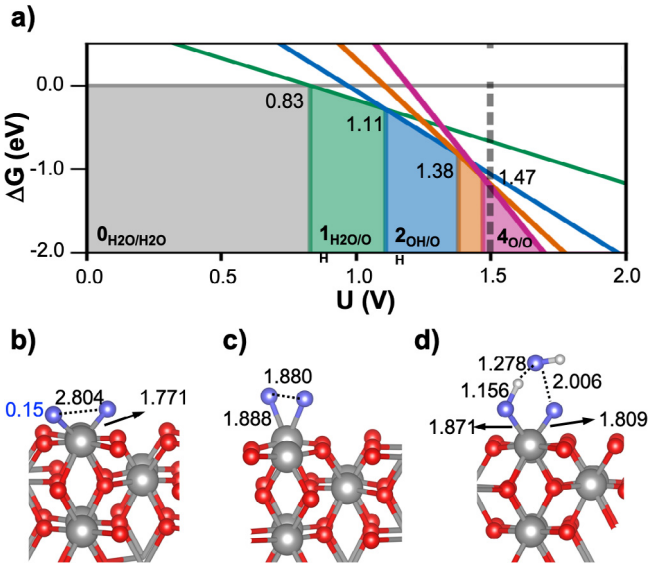

Fig. 6. a) Phase diagram of IrO_2 (001) surface at pH = 0, T = 298 K and P = 1 atm as function of the applied potential; b) Optimized structure for the Ir-bisoxo intermediate; c) Transition state structure associated with the oxo-coupling chemical process; d) Transition state associated with the WNA step. Values in blue correspond to the spin densities over the oxo groups. Distances in Å.

that are significantly larger than that of the single oxo group on the (001) facet and the magnetization reveals a certain oxyl character (Fig. 6b). As a consequence, the two chemical steps (oxo-coupling and water nucleophilic attack) are now easier than those occurring between two different centers. For the WNA mechanism, formation of $\mathbf{4_{OOH/OH}}$ is slightly endergonic (ΔG^0 = 0.25 eV) and the reaction presents a low Gibbs energy barrier ($\Delta G^{\ddagger}$ = 0.55 eV). Therefore, OER on the (001) is expected to take place involving Ir centers with two oxyl groups and through the WNA mechanism.

Fig. 7 and Figure S3 report the Gibbs energy profiles for the different surfaces of the whole catalytic process occurring through the water nucleophilic attack (Fig. 7) and the oxo–coupling mechanisms (Figure S3). Since the energy barriers for the proton coupled electron transfer steps are expected to be small as reported recently,[40] it is reasonable to assume that the largest Gibbs energy difference between two successive intermediates defines the required overpotential (η). In all cases, the computed overpotentials for the two reaction mechanisms are similar within each surface and thus, the applying mechanism is determined by the O-O bond formation step that it is likely rate-determining once the onset potential has been reached.[40] The energy barrier for the O-O bond formation suggests that the OER on the (110), (100) and (001) surfaces proceed through the WNA mechanism and the I2M pathway is preferred on the (011) surface. In these cases, the energy span at an applied potential of 1.5 V is small (between 0.33 and 0.55 eV). In the (011) surface, the spin density over the oxyl radicals is high and the interoxyl distance rather short,

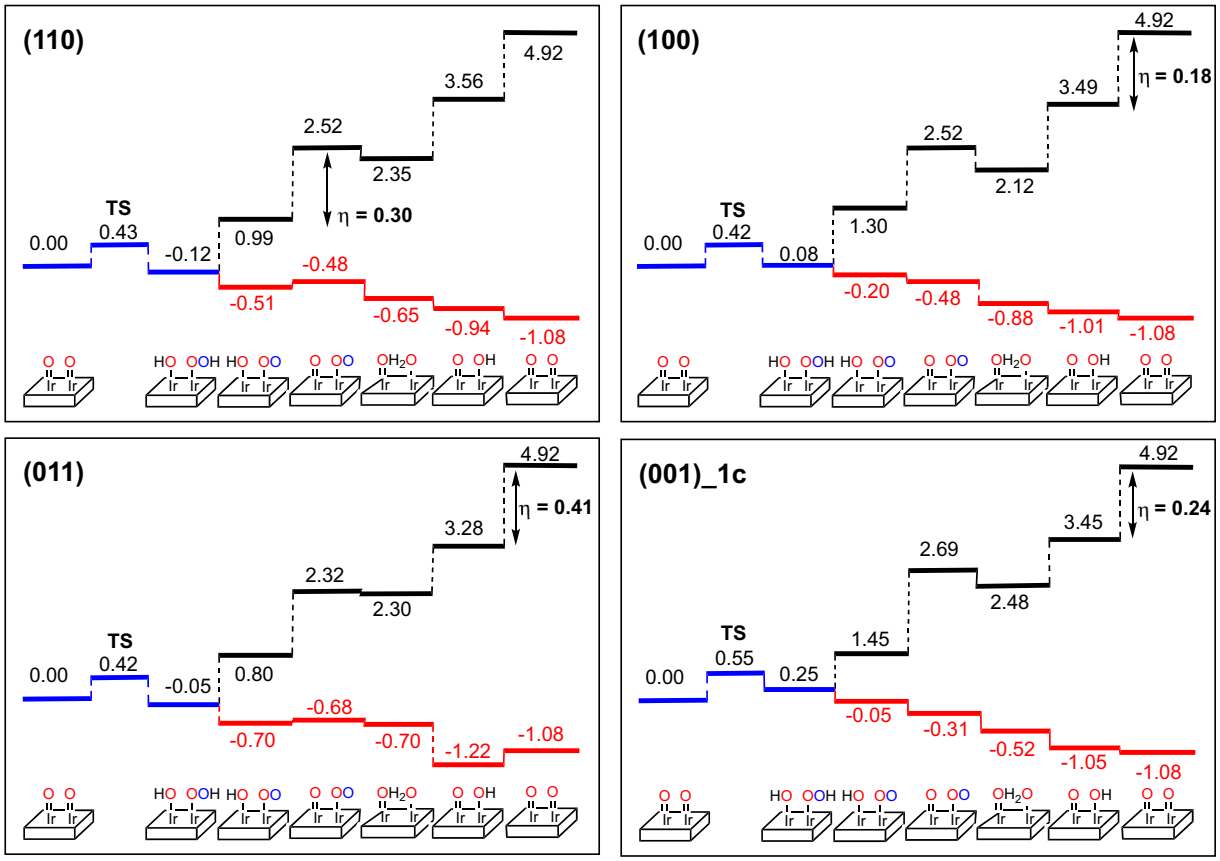

Fig. 7. Calculated Gibbs energy profile for the whole OER catalytic cycle through the water nucleophilic attack mechanism. Blue lines corresponds to the O-O bond formation, the black lines correspond to the energetics at an applied potential of 0 V and the red values are for an applied potential of 1.5 V.

which appears important for I2M mechanism to occur. The computed overpotentials are: 0.30, 0.41, 0.18 and 0.24 V for the (110), (011), (100) and (001) surfaces (Fig. 7). Moreover, the number of Ir vacant sites density varies as: (001) > (011) > (100) > (110) facet. Therefore, calculations predict that the highest activities per surface area would be obtained on the (100) and (001), as they require lower overpotentials for catalyzing the OER and they present a larger number of active sites per surface unit. In contrast, the (011) and (110) facets present either a smaller number of active sites per nm^2 or require higher overpotentials for catalyzing the process. These results reproduce the experimental trend when comparing the (100) and (110) surfaces[16] and suggest that (001) surface could be as reactive as the (100) facet.

Our results suggest that the reactivity on the different surfaces is highly controlled by two main factors. On one hand, the oxo-coupling and the water nucleophilic attack chemical steps are only feasible when surface Ir-O species has a significant oxyl character. Indeed, the computed energy barriers are highly determined by the spin density over the oxyl group and the interatomic distance between Ir-O species. At this point it is worth mentioning that, while the role of the oxyl character in determining the catalytic activity of molecular complexes[7,79–88] and first row transition metal oxides[89–95] has been discussed and shown to be important, its role in IrO_2 has been mainly eluded although oxyl species on IrO_2 has recently been detected by X-Ray spectroscopy. [58,96,97] According to our data, the IrO_2 surfaces and the Ir molecular analogues could have more similarities than one could initially suspect.

On the other hand, regardless of the considered surface, the overpotential required to perform the OER is determined by the oxidation of the Ir-OH hydroxyl group to Ir-O species ($\mathbf{3_{OH/O}}$ to $\mathbf{4_{O/O}}$ step or $\mathbf{5_{OO/OH}}$ to $\mathbf{6_{OO/O}}$), except if the process is so easy that the resulting species has no oxyl character. Indeed, the two factors are closely related and a subtle compromise between them is a key issue.

Analysis of the electronic structure of the four surfaces shows that the two variables are tuned by the coordination and nature of the vacant sites of the surface iridium centers. Unsaturated tetracoordinated centers are so poorly stabilized that the formation of one Ir=O group per metal center is easy. However, when this Ir=O group is formed on these centers, it does not have an oxyl character and thus it is not reactive. The oxidation of unsaturated pentacoordinated iridium centers is more challenging, the Ir-O group has a significant oxyl character and, consequently, they are more prone to react. When the vacant site is equatorial the Ir-O_L interaction is weaker than for the other cases and, overall, higher overpotentials are required. In contrast, the stronger Ir-O_L interaction at axial sites, leads to a good compromise between the oxyl character and oxidation feasibility. Oxidation of the tetracoordinated sites of the (001) surface to bisoxo species is as challenging as the oxidation of the (100) and (110) surfaces and the resulting species has enough oxyl character to undergo the WNA. Overall, this turns in very promising candidates that resembles the recently reported single-site Iridium species on ITO electrodes.[47]

4. Conclusions

The catalytic activity for the oxygen evolution reaction of the (110), (011), (100) and (001) main surfaces of rutile-like IrO_2 has been studied through spin-polarized PBE-D2 calculations. Both the oxo-coupling (I2M) and the water nucleophilic attack mechanisms have been considered and the energy barriers of the associated chemical processes calculated. Results show that the two mechanisms only take place when the Ir-O species on the surface has an oxyl character. In these cases, the water nucleophilic attack is always accessible and easy, while the oxo-coupling chemical step requires that the Ir-$O^{\bullet}$ radicals are also well-oriented. Overall, the water nucleophilic attack mechanism is preferred on the (110), (100) and (001) facets, while the I2M pathway is the main route on the (011) surface. The importance of oxyl groups on molecular or first row transition metal oxide catalysts has been outlined before.[7,81,83,91] Present results suggest that molecular and heterogeneous catalysts could have larger similarities than initially expected and thus strategies for catalyst development on molecular systems may also be suitable to improve heterogeneously catalyzed OER

The required overpotentials for the OER to occur on the four IrO_2 considered surfaces are determined by the feasibility to oxidize the Ir-OH species to Ir-O (either the $\mathbf{3_{O/OH}}$ to $\mathbf{4_{O/O}}$ step or the $\mathbf{5_{OO/OH}}$ to $\mathbf{6_{OO/O}}$ one). However, if the oxidation is too easy the resulting Ir=O species has no oxyl character and thus, does not further react. The iridium coordination and the nature of the vacant sites tunes both the oxidation ability and oxyl character. Tetracoordinated species are so unsaturated that formation of one Ir=O is easy, but the resulting species do not further react. Pentacoordinated centers with equatorial vacant sites are hardly oxidized to Ir=O, due to the weaker Ir-O_L interaction. The pentacoordinated centers with axial vacant sites show an intermediate behavior and they appear to be more active. Finally, tetracoordinated iridium sites on the (001) surface can be oxidized to bisoxo species able to perform OER at low potentials, which appears as promising candidates to be explored experimentally.

Funding

This work was supported by the Ministerio de Ciencia e Inovación MICINN [CTQ2017-89132-P]; the Generalitat de Catalunya [2017SGR1323] and Red Española de Supercomputación [QCM-2019–1-0043, QS-2019–2-0031].

Declaration of Competing Interest

The authors declared that there is no conflict of interest.

Acknowledgements

The authors gratefully acknowledge financial support from MICINN [CTQ2017-89132-P], the Generalitat de Catalunya [2017SGR1323] and Red Española de Supercomputación [QCM-2019-1-0043, QS-2019-2-0031]. XSM is grateful for the Professor Agregat Serra Húnter position.

Appendix A. Supplementary data

Supplementary data to this article can be found online at https://doi.org/10.1016/j.jcat.2021.02.026.

References

[1] R. Winkler-Goldstein, A. Rastetter, Green 3 (2013) 69–78.
[2] G. Gahleitner, Int. J. Hydrogen Energy 38 (2013) 2039–2061.
[3] L. Hammarström, Acc. Chem. Res. 42 (2009) 1859–1860.
[4] J.H. Montoya, L.C. Seitz, P. Chakthranont, A. Vojvodic, T.F. Jaramillo, J.K. Nørskov, Nat. Mater. 16 (2017) 70–81.
[5] C. Spöri, J.T.H. Kwan, A. Bonakdarpour, D.P. Wilkinson, P. Strasser, Angew. Chem. Int. Ed. 56 (2017) 5994–6021.
[6] M.G. Walter, E.L. Warren, J.R. McKone, S.W. Boettcher, Q. Mi, E.A. Santori, N.S. Lewis, Chem. Rev. 110 (2010) 6446–6473.
[7] X. Sala, S. Maji, R. Bofill, J. García-Antón, L. Escriche, A. Llobet, Acc. Chem. Res. 47 (2014) 504–516.
[8] M.D. Kärkäs, O. Verho, E.V. Johnston, B. Åkermark, Chem. Rev. 114 (2014) (2001) 11863–12001.
[9] J.D. Blakemore, R.H. Crabtree, G.W. Brudvig, Chem. Rev. 115 (2015) 12974–13005.
[10] B.M. Hunter, H.B. Gray, A.M. Müller, Chem. Rev. 116 (2016) 14120–14136.
[11] M.S. Burke, L.J. Enman, A.S. Batchellor, S. Zou, S.W. Boettcher, Chem. Mater. 27 (2015) 7549–7558.

[12] E. Fabbri, A. Habereder, K. Waltar, R. Kötz, T.J. Schmidt, Catal, Sci. Technol. 4 (2014) 3800–3821.
[13] T. Reier, H.N. Nong, D. Teschner, R. Schlögl, P. Strasser, Adv. Energy Mater. 7 (2017) 1601275.
[14] C.C.L. McCrory, S. Jung, I.M. Ferrer, S.M. Chatman, J.C. Peters, T.F. Jaramillo, J. Am. Chem. Soc. 137 (2015) 4347–4357.
[15] J. Yu, Q. He, G. Yang, W. Zhou, Z. Shao, M. Ni, ACS Catal. 9 (2019) 9973–10011.
[16] K.A. Stoerzinger, L. Qiao, M.D. Biegalski, Y. Shao-Horn, J. Phys. Chem. Lett. 5 (2014) 1636–1641.
[17] K.A. Stoerzinger, O. Diaz-Morales, M. Kolb, R.R. Rao, R. Frydendal, L. Qiao, X.R. Wang, N.B. Halck, J. Rossmeisl, H.A. Hansen, T. Vegge, I.E.L. Stephens, M.T.M. Koper, Y. Shao-Horn, ACS Energy Lett. 2 (2017) 876–881.
[18] H.-S. Oh, H.N. Nong, T. Reier, A. Bergmann, M. Gliech, J. Ferreira de Araújo, E. Willinger, R. Schlögl, D. Teschner, P. Strasser, J. Am. Chem. Soc. 138 (2016) 12552–12563.
[19] D.F. Abbott, D. Lebedev, K. Waltar, M. Povia, M. Nachtegaal, E. Fabbri, C. Copéret, T.J. Schmidt, Chem. Mater. 28 (2016) 6591–6604.
[20] O. Kasian, S. Geiger, T. Li, J.-P. Grote, K. Schweinar, S. Zhang, C. Scheu, D. Raabe, S. Cherevko, B. Gault, K.J.J. Mayrhofer, Energy Environ. Sci. 12 (2019) 3548–3555.
[21] J. Cheng, J. Yang, S. Kitano, G. Juhasz, M. Higashi, M. Sadakiyo, K. Kato, S. Yoshioka, T. Sugiyama, M. Yamauchi, N. Nakashima, ACS Catal. 9 (2019) 6974–6986.
[22] E. Willinger, C. Massué, R. Schlögl, M.G. Willinger, J. Am. Chem. Soc. 139 (2017) 12093–12101.
[23] Y. Sun, L. Yuan, Z. Liu, Q. Wang, K. Huang, S. Feng, Mater. Chem. Front. 3 (2019) 1779–1785.
[24] M. Povia, D.F. Abbott, J. Herranz, A. Heinritz, D. Lebedev, B.-J. Kim, E. Fabbri, A. Patru, J. Kohlbrecher, R. Schäublin, M. Nachtegaal, C. Copéret, T.J. Schmidt, Energy Environ. Sci. 12 (2019) 3038–3052.
[25] A. Minguzzi, O. Lugaresi, E. Achilli, C. Locatelli, A. Vertova, P. Ghigna, S. Rondinini, Chem. Sci. 5 (2014) 3591.
[26] H.G. Sanchez Casalongue, M.L. Ng, S. Kaya, D. Friebel, H. Ogasawara, A. Nilsson, Angew. Chem. Int. Ed. 53 (2014) 7169–7172.
[27] V. Pfeifer, T.E. Jones, J.J. Velasco Vélez, C. Massué, M.T. Greiner, R. Arrigo, D. Teschner, F. Girgsdies, M. Scherzer, J. Allan, M. Hashagen, G. Weinberg, S. Piccinin, M. Hävecker, A. Knop-Gericke, R. Schlögl, PCCP 18 (2016) 2292–2296.
[28] A.F. Pedersen, M. Escudero-Escribano, B. Sebok, A. Bodin, E. Paoli, R. Frydendal, D. Friebel, I.E.L. Stephens, J. Rossmeisl, I. Chorkendorff, A. Nilsson, J. Phys. Chem. B 122 (2018) 878–887.
[29] C.-J. Chang, Y.-C. Chu, H.-Y. Yan, Y.-F. Liao, H.M. Chen, Dalt. Trans. 48 (2019) 7122–7129.
[30] V. Pfeifer, T.E. Jones, J.J. Velasco Vélez, C. Massué, R. Arrigo, D. Teschner, F. Girgsdies, M. Scherzer, M.T. Greiner, J. Allan, M. Hashagen, G. Weinberg, S. Piccinin, M. Hävecker, A. Knop-Gericke, R. Schlögl, Surf. Interface Anal. 48 (2016) 261–273.
[31] P. Steegstra, M. Busch, I. Panas, E. Ahlberg, J. Phys. Chem. C 117 (2013) 20975–20981.
[32] N. Sivasankar, W.W. Weare, H. Frei, J. Am. Chem. Soc. 133 (2011) 12976–12979.
[33] S. Fierro, T. Nagel, H. Baltruschat, C. Comninellis, Electrochem. Commun. 9 (2007) 1969–1974.
[34] K. Macounova, M. Makarova, P. Krtil, Electrochem. Commun. 11 (2009) 1865–1868.
[35] H. Dau, C. Limberg, T. Reier, M. Risch, S. Roggan, P. Strasser, ChemCatChem 2 (2010) 724–761.
[36] E. Fabbri, T.J. Schmidt, ACS Catal. 8 (2018) 9765–9774.
[37] J. Rossmeisl, Z.-W. Qu, H. Zhu, G.-J. Kroes, J.K. Nørskov, J. Electroanal. Chem. 607 (2007) 83–89.
[38] Y.-H. Fang, Z.-P. Liu, J. Am. Chem. Soc. 132 (2010) 18214–18222.
[39] L.G.V. Briquet, M. Sarwar, J. Mugo, G. Jones, F. Calle-Vallejo, ChemCatChem 9 (2017) 1261–1268.
[40] C.F. Dickens, C. Kirk, J.K. Nørskov, J. Phys. Chem. C 123 (2019) 18960–18977.
[41] C.F. Dickens, J.K. Nørskov, J. Phys. Chem. C 121 (2017) 18516–18524.
[42] K. Klyukin, A. Zagalskaya, V. Alexandrov, J. Phys. Chem. C 123 (2019) 22151–22157.
[43] A. Zagalskaya, V. Alexandrov, J. Phys. Chem. Lett. 11 (2020) 2695–2700.
[44] A. Zagalskaya, V. Alexandrov, ACS Catal. 10 (2020) 3650–3657.
[45] R.R. Rao, M.J. Kolb, L. Giordano, A.F. Pedersen, Y. Katayama, J. Hwang, A. Mehta, H. You, J.R. Lunger, H. Zhou, N.B. Halck, T. Vegge, I. Chorkendorff, I.E.L. Stephens, Y. Shao-Horn, Nat. Catal. 3 (2020) 516–525.
[46] K. Klyukin, A. Zagalskaya, V. Alexandrov, J. Phys. Chem. C 122 (2018) 29350–29358.
[47] D. Lebedev, R. Ezhov, J. Heras-Domingo, A. Comas-Vives, N. Kaeffer, M. Willinger, X. Solans-Monfort, X. Huang, Y. Pushkar, C. Copéret, ACS Cent. Sci. 6 (2020) 1189–1198.
[48] S. Divanis, T. Kutlusoy, I.M. Ingmer Boye, I.C. Man, J. Rossmeisl, Chem. Sci. 11 (2020) 2943–2950.
[49] I.C. Man, H. Su, F. Calle-Vallejo, H.A. Hansen, J.I. Martínez, N.G. Inoglu, J. Kitchin, T.F. Jaramillo, J.K. Nørskov, J. Rossmeisl, ChemCatChem 3 (2011) 1159–1165.
[50] O. Piqué, F. Illas, F. Calle-Vallejo, PCCP 22 (2020) 6797–6803.
[51] S. Siahrostami, A. Vojvodic, J. Phys. Chem. C 119 (2015) 1032–1037.
[52] Z. Xu, J. Rossmeisl, J.R. Kitchin, J. Phys. Chem. C 119 (2015) 4827–4833.
[53] M. García-Melchor, L. Vilella, N. López, A. Vojvodic, ChemCatChem 8 (2016) 1792–1798.
[54] R.R. Rao, M.J. Kolb, N.B. Halck, A.F. Pedersen, A. Mehta, H. You, K.A. Stoerzinger, Z. Feng, H.A. Hansen, H. Zhou, L. Giordano, J. Rossmeisl, T. Vegge, I. Chorkendorff, I.E.L. Stephens, Y. Shao-Horn, Energy Environ. Sci. 10 (2017) 2626–2637.
[55] Y. Ping, R.J. Nielsen, W.A. Goddard, J. Am. Chem. Soc. 139 (2017) 149–155.
[56] E. Watanabe, H. Ushiyama, K. Yamashita, Y. Morikawa, D. Asakura, M. Okubo, A. Yamada, J. Phys. Chem. C 121 (2017) 18975–18981.
[57] J.A. Gauthier, C.F. Dickens, L.D. Chen, A.D. Doyle, J.K. Nørskov, J. Phys. Chem. C 121 (2017) 11455–11463.
[58] H.N. Nong, L.J. Falling, A. Bergmann, M. Klingenhof, H.P. Tran, C. Spöri, R. Mom, J. Timoshenko, G. Zichittella, A. Knop-Gericke, S. Piccinin, J. Pérez-Ramírez, B.R. Cuenya, R. Schlögl, P. Strasser, D. Teschner, T.E. Jones, Nature 587 (2020) 408–413.
[59] J. Heras-Domingo, M. Sodupe, X. Solans-Monfort, J. Phys. Chem. C 123 (2019) 7786–7798.
[60] D. González, J. Heras-Domingo, S. Pantaleone, A. Rimola, L. Rodríguez-Santiago, X. Solans-Monfort, M. Sodupe, ACS Omega 4 (2019) 2989–2999.
[61] G. Kresse, J. Hafner, Phys. Rev. B 47 (1993) 558–561.
[62] G. Kresse, J. Furthmüller, Phys. Rev. B 54 (1996) 11169–11186.
[63] J.P. Perdew, K. Burke, M. Ernzerhof, Phys. Rev. Lett. 77 (1996) 3865–3868.
[64] S. Grimme, J. Comput. Chem. 25 (2004) 1463–1473.
[65] P.E. Blöchl, Phys. Rev. B 50 (1994) 17953–17979.
[66] G. Kresse, D. Joubert, Phys. Rev. B 59 (1999) 1758–1775.
[67] H.J. Monkhorst, J.D. Pack, Phys. Rev. B 13 (1976) 5188–5192.
[68] D. González, B. Camino, J. Heras-Domingo, A. Rimola, L. Rodríguez-Santiago, X. Solans-Monfort, M. Sodupe, J. Phys. Chem. C 124 (2020) 1227–1237.
[69] K. Mathew, R. Sundararaman, K. Letchworth-Weaver, T.A. Arias, R.G. Hennig, J. Chem. Phys. 140 (2014), 084106.
[70] G. Henkelman, B.P. Uberuaga, H. Jónsson, J. Chem. Phys. 113 (2000) 9901–9904.
[71] G. Henkelman, H. Jónsson, J. Chem. Phys. 113 (2000) 9978–9985.
[72] R. Mu, D.C. Cantu, X. Lin, V.-A. Glezakou, Z. Wang, I. Lyubinetsky, R. Rousseau, Z. Dohnálek, J. Phys. Chem. Lett. 5 (2014) 3445–3450.
[73] M.-T. Nguyen, R. Mu, D.C. Cantu, I. Lyubinetsky, V.-A. Glezakou, Z. Dohnálek, R. Rousseau, J. Phys. Chem. C 121 (2017) 18505–18515.
[74] R.R. Rao, M.J. Kolb, J. Hwang, A.F. Pedersen, A. Mehta, H. You, K.A. Stoerzinger, Z. Feng, H. Zhou, H. Bluhm, L. Giordano, I.E.L. Stephens, Y. Shao-Horn, J. Phys. Chem. C 122 (2018) 17802–17811.
[75] C.J. Cramer, W.B. Tolman, K.H. Theopold, A.L. Rheingold, Proc. Natl. Acad. Sci. 100 (2003) 3635–3640.
[76] P.L. Holland, Dalt. Trans. 39 (2010) 5415.
[77] We also explored the possibility that the water attack occurs at 3OH/O in the (011) surface. However, we were unable to find any minimum of 3OOH/H2O, thus suggesting that 3OH/O has to be oxidized before to 4O/O.
[78] We also considered the possibility that process involves H from hydroxyl, but the computed energies are similar or higher (see Supplementary Materials).
[79] P.E.M. Siegbahn, R.H. Crabtree, J. Am. Chem. Soc. 121 (1999) 117–127.
[80] L.-P. Wang, T. Van Voorhis, J. Phys. Chem. Lett. 2 (2011) 2200–2204.
[81] G. Mattioli, P. Giannozzi, A. Amore Bonapasta, L. Guidoni, J. Am. Chem. Soc. 135 (2013) 15353–15363.
[82] D.W. Crandell, S. Xu, J.M. Smith, M.-H. Baik, Inorg. Chem. 56 (2017) 4435–4445.
[83] P.E.M. Siegbahn, Acc. Chem. Res. 42 (2009) 1871–1880.
[84] X. Yang, M.-H. Baik, J. Am. Chem. Soc. 128 (2006) 7476–7485.
[85] K.R. Yang, A.J. Matula, G. Kwon, J. Hong, S.W. Sheehan, J.M. Thomsen, G.W. Brudvig, R.H. Crabtree, D.M. Tiede, L.X. Chen, V.S. Batista, J. Am. Chem. Soc. 138 (2016) 5511–5514.
[86] D.W. Shaffer, Y. Xie, J.J. Concepcion, Chem. Soc. Rev. 46 (2017) 6170–6193.
[87] L. Duan, F. Bozoglian, S. Mandal, B. Stewart, T. Privalov, A. Llobet, L. Sun, Nat. Chem. 4 (2012) 418–423.
[88] C.N. Brodsky, R.G. Hadt, D. Hayes, B.J. Reinhart, N. Li, L.X. Chen, D.G. Nocera, Proc. Natl. Acad. Sci. 114 (2017) 3855–3860.
[89] C.Y. Cummings, F. Marken, L.M. Peter, K.G. Upul Wijayantha, A.A. Tahir, J. Am. Chem. Soc. 134 (2012) 1228–1234.
[90] B. Klahr, T. Hamann, J. Phys. Chem. C 118 (2014) 10393–10399.
[91] D.M. Herlihy, M.M. Waegele, X. Chen, C.D. Pemmaraju, D. Prendergast, T. Cuk, Nat. Chem. 8 (2016) 549–555.
[92] J.G. McAlpin, T.A. Stich, C.A. Ohlin, Y. Surendranath, D.G. Nocera, W.H. Casey, R. D. Britt, J. Am. Chem. Soc. 133 (2011) 15444–15452.
[93] D.K. Bediako, C. Costentin, E.C. Jones, D.G. Nocera, J.-M. Savéant, J. Am. Chem. Soc. 135 (2013) 10492–10502.
[94] X. Chen, S.N. Choing, D.J. Aschaffenburg, C.D. Pemmaraju, D. Prendergast, T. Cuk, J. Am. Chem. Soc. 139 (2017) 1830–1841.
[95] A.M. Ullman, C.N. Brodsky, N. Li, S.-L. Zheng, D.G. Nocera, J. Am. Chem. Soc. 138 (2016) 4229–4236.
[96] L.J. Frevel, R. Mom, J.-J. Velasco-Vélez, M. Plodinec, A. Knop-Gericke, R. Schlögl, T.E. Jones, J. Phys. Chem. C 123 (2019) 9146–9152.
[97] Z. Pavlovic, C. Ranjan, M. van Gastel, R. Schlögl, Chem. Commun. 53 (2017) 12414–12417.